



# Deformation behaviour of ion-irradiated FeCr: A nanoindentation study

Kay Song<sup>1,a)</sup> , Hongbing Yu<sup>2</sup> , Phani Karamched<sup>3</sup> , Kenichiro Mizohata<sup>4</sup> ,  
David E. J. Armstrong<sup>3</sup> , Felix Hofmann<sup>1</sup> 

<sup>1</sup>Department of Engineering Science, University of Oxford, Parks Road, Oxford OX1 3PJ, UK

<sup>2</sup>Canadian Nuclear Laboratories, Chalk River, ON K0J 1J0, Canada

<sup>3</sup>Department of Materials, University of Oxford, Parks Road, Oxford OX1 3PH, UK

<sup>4</sup>University of Helsinki, P.O. Box 64, 00560 Helsinki, Finland

<sup>a)</sup> Address all correspondence to this author. e-mail: kay.song@eng.ox.ac.uk

Received: 6 January 2022; accepted: 26 May 2022; published online: 21 June 2022

Understanding the mechanisms of plasticity in structural steels is essential for the operation of next-generation fusion reactors. This work on the deformation behaviour of FeCr, focusses on distinguishing the nucleation of dislocations to initiate plasticity, from their propagation through the material. Fe3Cr, Fe5Cr, and Fe10Cr were irradiated with 20 MeV Fe<sup>3+</sup> ions at room temperature to doses of 0.008 dpa and 0.08 dpa. Nanoindentation was then carried out with Berkovich and spherical indenter tips. Our results show that the nucleation of dislocations is mainly from pre-existing sources, which are not significantly affected by the presence of irradiation defects or Cr%. Yield strength, an indicator of dislocation mobility, increases with irradiation damage and Cr content, while work hardening capacity decreases mainly due to irradiation defects. The synergistic effects of Cr and irradiation damage in FeCr appear to be more important for the propagation of dislocations than for their nucleation.

## Introduction

Reduced activation ferritic/martensitic (RAFM) steels are prime candidate materials for structural components of next-generation nuclear fusion and fission reactors [1]. They are favoured over austenitic steels for their resistance to irradiation swelling and helium embrittlement, and good thermomechanical properties [2, 3]. For the safe and efficient operation of reactors, the impact of the reactor environment, mainly the effect of neutron irradiation, on the behaviour of the reactor materials must be well-understood. For the structural components of the reactor, it is particularly important to characterise the irradiation-induced evolution of mechanical properties and the onset of plasticity.

The study of FeCr binary alloy materials is useful for gaining mechanistic insight into the effects of irradiation on RAFM steels as they reduce the microstructural complexity associated with numerous minor alloying elements in industrial steels [4, 5]. In particular for comparisons with theoretical simulations, which are crucial for prediction of material properties in operation but not yet able to capture complex RAFM steels, the experimental study of pure Fe and FeCr model binary alloy provides vital information [6, 7].

Ion-irradiation is a useful surrogate for simulating the damage caused by neutron irradiation [8]. It allows the accumulation of large damage doses, in a controlled environment, over a short span of time without inducing transmutation [9]. This is particularly useful for comparisons with neutron damage that produce dense defect cascades [10]. Ion-irradiation eliminates transmutation-induced evolution in the chemical composition of the samples and allows for comparison to simulations [11, 12]. The drawback of ion-irradiation is that the damage layer produced is only a few microns thick, which necessitates the use of specialised techniques to characterise material properties at this scale.

Nanoindentation has proved to be invaluable for providing mechanical information of ion-irradiation damaged materials as it can extract mechanical information from the thin irradiated layer [13–15]. It has been used to investigate mechanical properties including yield strength, deformation behaviour and elastic properties [16, 17].

Irradiated Fe and Fe-based alloys exhibit hardening and embrittlement due to the formation of point defects, dislocation loops, and clusters acting as barriers to dislocation movement

[18, 19]. Changes in mechanical properties (e.g. yield strength) can be measured even at very low damage levels ( $10^{-4}$  displacements-per-atom, dpa) when defects are not yet visible with electron microscopy [20, 21]. This makes insights from mechanical characterisation valuable. Previous nanoindentation studies on irradiated FeCr largely focused on quantifying irradiation-induced hardening behaviour [13, 17, 22, 23]. The amount of hardening has been found to increase with Cr content for doses below 1 dpa [13, 24]. There exists some experimental work on the deformation behaviour of irradiated FeCr, particularly after the onset of yield, with strain softening commonly observed [14, 25, 26]. An unanswered question from the current literature is the behaviour just before and at the onset of pop-in when the dominant effects are dislocation nucleation and multiplication. The effect of irradiation on the mechanisms responsible for the initiation of plasticity in FeCr is also currently unclear. Both the initiation and progression of plasticity are crucial to predicting the structural integrity of steel components during operation.

A second aspect unexplored in existing studies is the synergistic effect of Cr and irradiation damage on the initiation and progression of plasticity in FeCr. Many existing studies [14, 27, 28] have focused on only one composition of Cr% or one dose. This makes conclusions about the effect of Cr content and dose level hard to reach, as samples from different studies vary in processing history, irradiation condition and data analysis protocol. From our previous study of irradiated FeCr [24], we found that enhanced defect retention from the presence of Cr caused greater changes in the hardness, thermal diffusivity and lattice strain. The present study follows on from these previous results to focus on the synergistic effects of Cr and irradiation dose on the deformation behaviour of irradiated FeCr.

The study of Fe and FeCr binary alloys at room temperature, as opposed to more commonly at 500–800 K is important for fundamental understanding of irradiation damage. Atomistic simulations of non-thermally activated processes, e.g. stress-driven defect evolution, are important and can only be compared to experimental results obtained in the ‘low temperature’ regime [29, 30]. This is an important step to understanding irradiation damage at reactor operation temperatures where both thermally activated and stress-driven processes are at play. Defect microstructures in Fe and Fe-based alloys have been found to evolve on a timescale of weeks to months [31, 32] at low temperatures  $T < 600$  K, and this timescale decreases exponentially with increasing temperature [33]. Therefore, irradiating and characterising at room temperature, or below, prolongs the timespan over which defect microstructures do not evolve significantly and ensures the material properties characterised after the irradiation are representative of the defects created during irradiation conditions.

We systematically examine the deformation behaviour of FeCr with nanoindentation as a function of Cr content (3, 5,

and 10%), and damage level (unimplanted, 0.008, and 0.08 dpa). Irradiation and mechanical characterisation were carried out at room temperature. Nanoindentation reveals the dose- and composition-dependent behaviour of dislocation nucleation and propagation in the irradiated regions of the materials to provide insights into the early stage deformation behaviour of irradiated FeCr. The use of indenter tips with different effective radii makes it possible to distinguish between dislocation nucleation and propagation in these measurements. Our findings are discussed in light of previous experimental and ab initio studies of Fe and FeCr. This information is crucial for the design and performance prediction of structural components in future reactors.

## Results

### Initiation of plasticity: pop-in analysis

All samples were indented with a Berkovich tip and two spherical tips with nominal radii of 1 and 5  $\mu\text{m}$  (further details given in Sect. 4.2 of Methods and Materials). The use of different tip sizes allows distinction between different sources of dislocation nucleation, as further discussed below.

A typical load vs. displacement curve measured in this experiment is shown in Fig. 1. The first section of the curve [Fig. 1(a)] between points A and B is the elastic Hertzian response which can be described as the contact between a sphere (the indenter tip) and an elastic half-space (the sample surface) [34]:

$$P = \frac{4}{3} E_r R^{\frac{1}{2}} h_e^{\frac{3}{2}} \quad (1)$$

where  $P$  is the applied load,  $R$  is the radius of the sphere, and  $h_e$  is the elastic indentation depth.  $E_r$  is the reduced modulus given by:

$$\frac{1}{E_r} = \frac{1 - \nu_i^2}{E_i} + \frac{1 - \nu_s^2}{E_s} \quad (2)$$

where  $E$  is the elastic modulus and  $\nu$  is Poisson’s ratio, with subscripts  $i$  and  $s$  referring to the indenter and the sample, respectively. Here, we used  $E_i = 1140$  GPa,  $\nu_i = 0.07$  [35] for the diamond indenter tips and  $\nu_s = 0.29$  for the FeCr alloys [36]. From our previous nanoindentation study [24],  $E_s$  was found to be 218 GPa for Fe3Cr and Fe5Cr, and 228 GPa for Fe10Cr.

The method proposed by Leitner et al. [37] was used to fit the radii of the tips in this study. This method fits the contact area and contact depth of the indentation, rather than the total depth. The elastic portion (between points A to B in Fig. 1) from indentation of pure unimplanted Fe ( $E_s = 204$  GPa) was used for the fitting. For the purposes of this work, an effective radius ( $R_{\text{eff}}$ ) was calculated from the fitting by approximating the tips as spherical. For the Berkovich tip, this assumption is only valid for small indentation depths (further discussed in

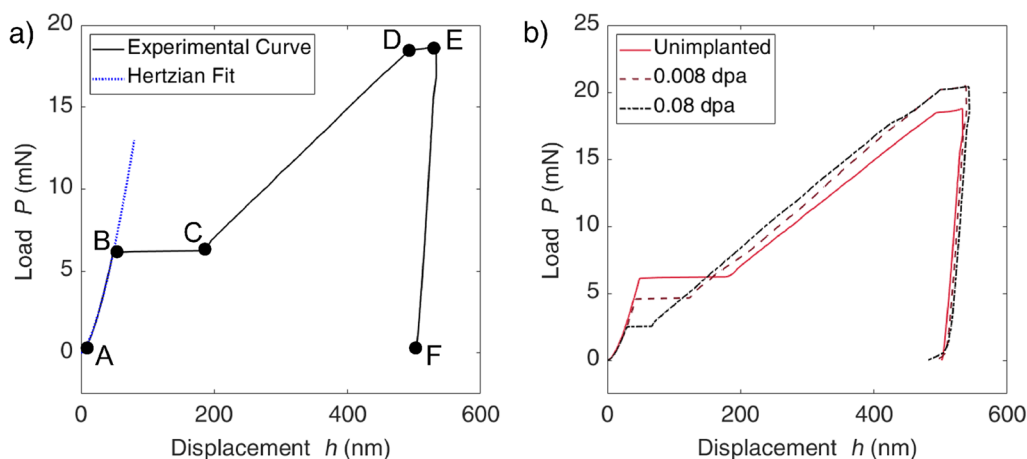


**Figure 1:** The load–displacement curve of the indentation of Fe3Cr with a nominally 5  $\mu\text{m}$  radius spherical tip. (a) The indentation curve of unirradiated Fe3Cr with key segments labelled: elastic deformation described by Hertzian mechanics (A  $\rightarrow$  B), pop-in (B  $\rightarrow$  C), elastic-plastic deformation (C  $\rightarrow$  D) and creep (D  $\rightarrow$  E). (b) The effect of irradiation on decreasing the pop-in loads for Fe3Cr.

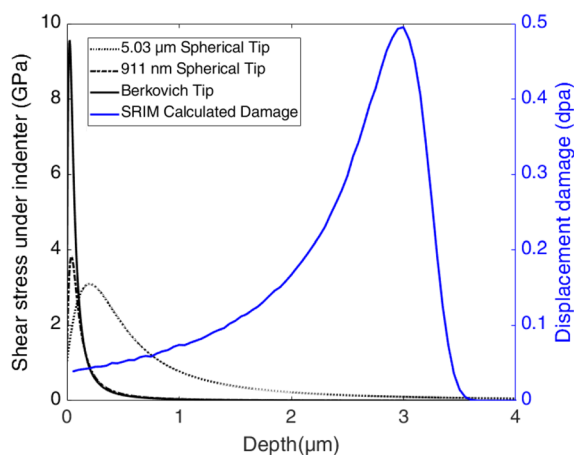


**Figure 2:** The principle shear stress directly ahead of the indenter tip at the onset of pop-in for Fe10Cr irradiated to 0.08 dpa (black traces). The stress distribution in each case is computed using the corresponding  $P_{\text{pop}}$  load. The size of the highly stressed zone increases with tip size but are all still contained in the irradiated region (blue trace).

text related to Fig. 3), making use of the rounding of the tip. The  $R_{\text{eff}}$  for the Berkovich tip was found to be  $120 \pm 31$  nm. The spherical tips were found to have effective radii of  $911 \pm 122$  nm and  $5.03 \pm 0.53$   $\mu\text{m}$ . Note, the manufacturer reported  $1.11 \pm 0.04$  and  $4.83 \pm 0.24$   $\mu\text{m}$ , respectively, for the spherical indenter tips.

A ‘pop-in’ occurs between points B and C [Fig. 1(a)], and the pop-in load (at point B),  $P_{\text{pop}}$  was identified for all samples. The presence of ‘pop-in’s correspond to the initiation of plasticity and can either be from nucleating new dislocations or mobilising pre-existing dislocations [38]. These two different mechanisms can be distinguished using indenter tips with different radii. Further details are given in the text surrounding Fig. 2.

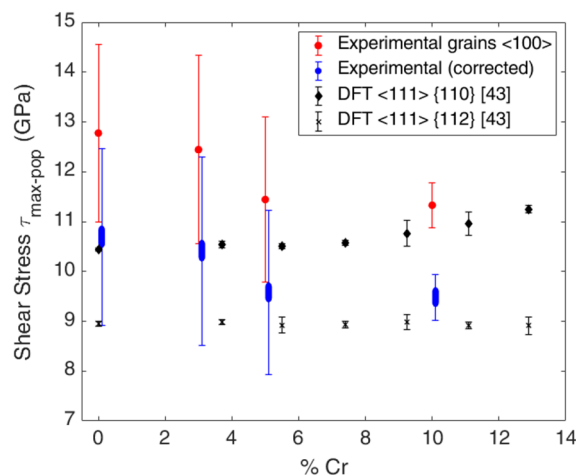


**Figure 3:** The maximum shear stress at the onset of pop-in ( $\tau_{\text{max-pop}}$ ) under the Berkovich indenter tip ( $R_{\text{eff}} = 120$  nm) for unimplanted FeCr with different levels of Cr% for grains of near {100} out-of-plane orientation (red circles), where the primary slip system is {111}{110}. The error bars show one standard deviation of the measurements. Density functional theory (DFT) calculations (black diamonds and crosses) [43] are included for comparison. A range of possible corrections have been applied to correlate the experimentally measured shear stress to theoretical calculations (blue), explanations are provided in the corresponding text.

Elastic-plastic deformation (between points C and D) occurs following a pop-in event as dislocations have been nucleated in the material. Sample creep can also be observed between points D and E when the indenter is held at the maximum load for 10 s.

The use of tips with different effective radii creates differently sized stress zones underneath the surface. The principal shear stress ( $\tau$ ) directly ahead of the indenter tip in the sample before the occurrence of pop-ins was computed using Hertzian contact mechanics [34]:

$$\tau = \frac{1}{2}p_0 \left[ (1+\nu) \left( 1 - \left( \frac{z}{a} \right) \arctan \left( \frac{a}{z} \right) \right) - \frac{3}{2} \left( \frac{1}{1+z^2/a^2} \right) \right] \quad (3)$$

where  $z$  is the coordinate into the material normal to the surface, and  $a$  is the contact radius (see Eq. 7).  $p_0$  is given by [34]:

$$p_0 = \left( \frac{6P_{\text{pop}}E_r^2}{\pi^3 R^2} \right)^{\frac{1}{3}}. \quad (4)$$

The maximum shear stress under the indenter experienced by the sample at the onset of pop-ins,  $\tau_{\text{max-pop}}$ , is then given by [34]:

$$\tau_{\text{max-pop}} = 0.31p_0. \quad (5)$$

The load at the onset of the pop-in event ( $P_{\text{pop}}$ ) was identified for all the load-displacement curves recorded. In the case of multiple pop-ins,  $P_{\text{pop}}$  was taken at the first pop-in event. The principal shear stress as a function of depth for different indenter tip radii was then calculated using Eqs. 3 and 4. Figure 2 shows this for the Fe10Cr sample irradiated to 0.08 dpa, but the features are representative of all the samples in this study. As the tip radius increases, the stressed zone extends deeper into the material. We consider a ‘main stressed zone’ as the depth range where the shear stress,  $\tau$ , experienced is at least 50% of  $\tau_{\text{max-pop}}$ . Even for the largest tip, 5.03  $\mu\text{m}$  spherical, the main stressed zone is still fully contained within the ion-irradiated layer.

From Fig. 2, it can be seen that  $\tau_{\text{max-pop}}$  (the peak height) decreases with increasing tip size. This has also been observed previously in nickel [39], tungsten [40] and molybdenum [41]. This size-dependent phenomenon originates from the initiation of plasticity following either the nucleation of dislocations or the activation of existing dislocations (e.g. Frank–Read sources) in the material. The former mechanism requires shearing the crystal lattice to generate dislocations and hence generally requires a much higher applied stress than the latter mechanism, which relies on unlocking pre-existing dislocations. Since the volume of the highly stressed zone scales with the indenter radius (Fig. 2), the probability of encountering a pre-existing dislocation is higher in the highly stressed zone under a larger indenter, compared to applying the same load to a smaller indenter. This means that for a larger indenter plasticity most likely can be initiated once the applied stress is large enough to mobilise pre-existing defects [39]. For a smaller indenter it is more likely that plasticity is initiated when the applied stress is greater than the ideal strength of the material, so that new shear dislocation loops can be nucleated before the highly stressed zone grows large enough to encounter a pre-existing dislocation source with a lower activation barrier.

The  $\tau_{\text{max-pop}}$  for loading with a Berkovich tip for the unimplanted materials is calculated using Eqs. 4 and 5 (Fig. 3). In the small, relatively defect-free volume probed by the sharp Berkovich tip,  $\tau_{\text{max-pop}}$  should approach the theoretical shear strength.

This is because it can be assumed that for the indentation depths at which pop-in's occur for a Berkovich tip (< 20 nm), the contribution of pre-existing defects is negligible due to the highly localised stress fields. This has also been previously observed in several other material systems [39, 42]. Experimental values shown in Fig. 3 are from indentation of grains with close to (100) out-of-plane orientation, and the main corresponding slip system is {111}{110}. In our study, the experimental  $\tau_{\text{max-pop}}$  is within 20% of the theoretical shear strength predicted by density functional theory calculations [43].

The discrepancy between the experimental and theoretical results in Fig. 3 can be attributed to two main factors: The first is that the *ab initio* calculations do not account for the triaxiality of the stress state beneath the indenter. This raises the ideal shear stress compared to the assumption made in [43] of a fully relaxed shear load. Revised *ab initio* analysis of W and Mo [44] showed that modelling a triaxial stress state will produce a theoretical shear strength that is 6–13% higher than the fully relaxed model. Furthermore, the maximum shear stress obtained by the Hertzian contact model (Eqs. 4 and 5) assumes that the contact area is small compared to the size of the elastic bodies in contact [34]. This assumption does not fully stand near the yield point. From FEM analysis [44], it is reported that the maximum shear stress calculated from the Hertzian contact model overestimates the true stress by up to 20% for a large range of metals. These factors mean that the maximum shear stress obtained by nanoindentation overestimates the theoretical results by 17 to 22%. The blue points in Fig. 3 show the range of corrected theoretical shear strength values for each Cr content applied according to the analysis of Krenn et al. [44]. These corrected experimental values are in better agreement with the theoretical values.

The average  $\tau_{\text{max-pop}}$  shows a weak decreasing trend with increasing Cr content. However, the changes are within the experimental uncertainties of this study and further investigation would be helpful to identify underlying mechanisms. The effect of alloying elements on the theoretical strength of materials has been previously investigated in theoretical studies, for example in titanium [45] and silicon [46], and depends strongly on both the matrix and solute. A previous experimental study of the shear modulus ( $G$ ), which is proportional to theoretical strength, of Fe and FeCr alloys showed a small increase ( $\leq 5\%$ ) with Cr content between Fe and Fe10Cr [47]. However, a further study reported a minimum value of  $G$  at Cr% = 5% [48].

For indentation with a Berkovich tip, the effect of ion-irradiation on pop-in load, and thus  $\tau_{\text{max-pop}}$ , can be seen in Fig. 4. The pop-in loads were not found to vary systematically between grains of near (100), (110) and (111) out-of-plane orientations, and from here on, results from all orientations are considered together.

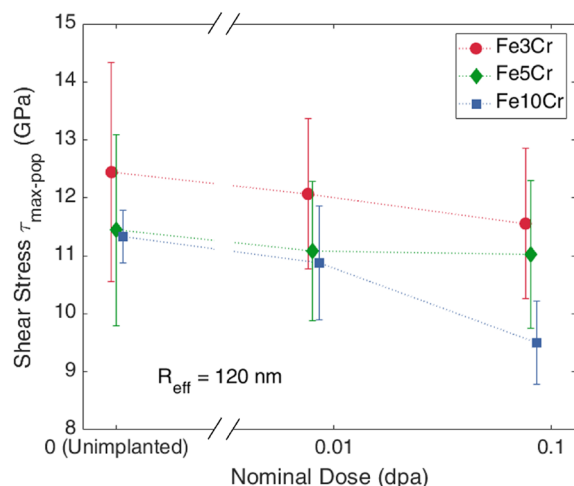


**Figure 4:** The maximum shear stress under the Berkovich indenter tip at the onset of pop-in ( $\tau_{\text{max-pop}}$ ) for Fe3Cr (red circle), Fe5Cr (green diamond) and Fe10Cr (blue square) as a function of dose. The error bars show one standard deviation of the measurements.

The decrease in  $\tau_{\text{max-pop}}$  with irradiation dose can be rationalised by considering irradiation-induced defects in the material as sites for heterogeneous dislocation nucleation. From TEM studies of FeCr materials produced under identical protocols, the defects caused by ion-irradiation at room temperature consist of dislocation loops with Burger's vector  $\frac{1}{2}a_0\langle 111 \rangle$  or  $a_0\langle 100 \rangle$  [49]. It has been shown before, in Ni-irradiated Mo, that ion-irradiation-induced defects serve as local instabilities, which decrease the shear stress required for dislocation nucleation [50]. This differs from other pop-in studies which investigated materials damaged by mechanical straining, where

the main form of heterogeneous dislocation nucleation is from Frank–Read sources with much lower activation barriers than irradiation-induced defects [51]. It also appears that the effect of Cr content (Fig. 4) on the change in  $\tau_{\text{max-pop}}$  is greater than the effect of increasing irradiation dose alone. The change in  $\tau_{\text{max-pop}}$  for Fe3Cr and Fe5Cr following irradiation to 0.08 dpa is less than the change in  $\tau_{\text{max-pop}}$  due to the increase in Cr% from 3 to 5%. Furthermore, Fe3Cr consistently has the largest  $\tau_{\text{max-pop}}$  for all irradiation doses. Even the Fe3Cr sample irradiated to 0.08 dpa still has higher  $\tau_{\text{max-pop}}$  than the unirradiated Fe5Cr and Fe10Cr samples.

The synergistic effect of Cr% and irradiation dose level can be seen in the greater decrease of  $\tau_{\text{max-pop}}$  for Fe10Cr compared to Fe3Cr and Fe5Cr following irradiation. This can be attributed to greater retention of irradiation-induced defects in the presence of Cr atoms [52, 53]. The irradiation-induced change of other material properties such as hardening, decrease in thermal diffusivity and increase in irradiation strain has also been found to be greater for higher Cr% in ion-irradiated FeCr [24].

For indentation performed with larger spherical tips ( $R_{\text{eff}} = 911 \text{ nm}$  and  $5.03 \mu\text{m}$ ), pop-ins were still noticeable in both the reference (unirradiated) and irradiated samples.  $\tau_{\text{max-pop}}$  for these spherical tips are shown in Fig. 5. Indenting with the spherical tips reveals a reduction in  $\tau_{\text{max-pop}}$  with increasing dose for Fe3Cr. For Fe5Cr, this is seen for indentation with  $R_{\text{eff}} = 911 \text{ nm}$ . This is similar to the observations from the Berkovich indentation pop-ins in Figure 4.

For spherical tips, the  $\tau_{\text{max-pop}}$  measured are all significantly lower than those for the Berkovich tip. This drop in  $\tau_{\text{max-pop}}$  for increased tip radius is much larger than the reduction in

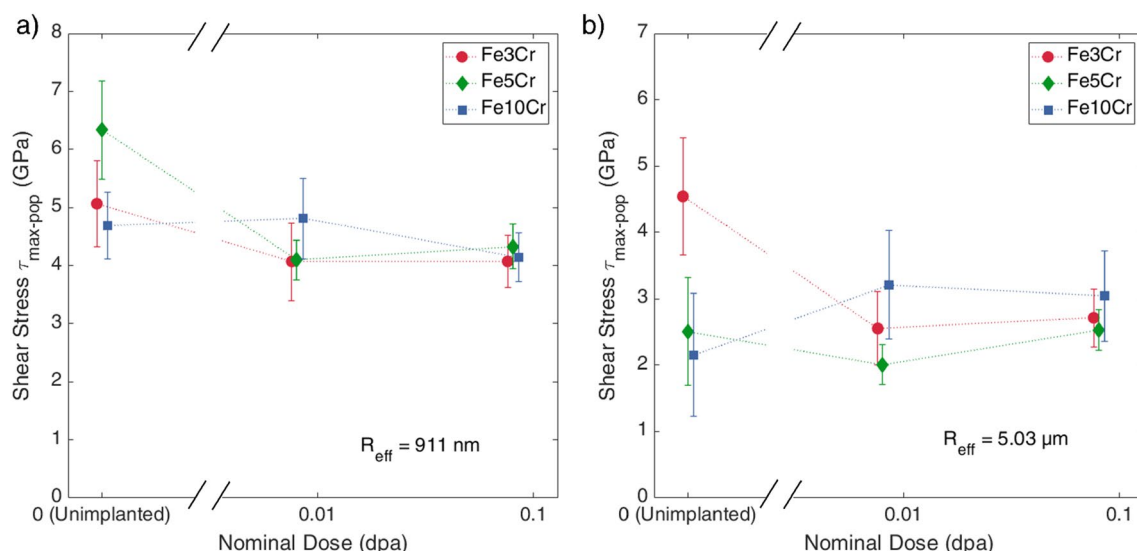


**Figure 5:** The maximum shear stress under the indenter tip ( $\tau_{\text{max-pop}}$ ) at the onset of pop-in for Fe3Cr (red circle), Fe5Cr (green diamond) and Fe10Cr (blue square) as a function of dose for spherical indenters with effective radii (a) 911 nm and (b) 5.03  $\mu\text{m}$ . The error bars show one standard deviation of the measurements.



$\tau_{\text{max-pop}}$  following irradiation (Figs. 4 and 5). This suggests that the dislocation nucleation sources probed during indentation with larger tips have lower activation barriers than dislocation nucleation from irradiation-induced defects. Hence, the dislocation nucleation during indentation using tips with larger radii must be from sources other than irradiation-induced defects, such as other pre-existing dislocations.

The use of indenter tips with different radii makes it possible to begin to separate the contribution of Cr content and irradiation dose to the different mechanisms involved in plasticity initiation. The nucleation of dislocations by shearing the lattice was examined by exceeding the theoretical shear strength of the material using Berkovich indentation (Figs. 3 and 4). The operation of pre-existing dislocation sources (e.g. Frank–Read sources) plays a much more prominent role in indentation with larger spherical tips, due to the lower activation energy required. Our results (Fig. 5) show that  $\tau_{\text{max-pop}}$  varies little with Cr content and irradiation dose, but rather is much more dependent on the size of the spherical tip. This is due to a larger tip being able to probe a bigger high-stress zone and initiate plasticity from pre-existing sources.

For Fe10Cr,  $\tau_{\text{max-pop}}$  increases following irradiation when probed by a spherical tip with  $R_{\text{eff}} = 5.03 \mu\text{m}$  [Fig. 5(b)]. This is different to the dependence of  $\tau_{\text{max-pop}}$  on irradiation dose in all other samples which either showed a decrease or no change in  $\tau_{\text{max-pop}}$  with irradiation. This may point to a more complex behaviour of dislocation nucleation following irradiation, possibly a combination of effects from irradiation-induced dislocation sources and pre-existing sources now sampled by indenting with a larger tip. The other possible explanation is that the unimplanted Fe10Cr material possesses an unusually high level of pre-existing dislocations, which leads to a particularly low  $\tau_{\text{max-pop}}$  required for the initiation of plasticity. To clarify this point, we examine the pre-existing defect concentrations in the sample with electron microscopy.

### Determining pre-existing dislocation density

High-resolution electron backscatter diffraction (HR-EBSD) measurements were used to measure geometrically necessary dislocation (GND) density on the surface of the samples [54]. Cross-correlation analysis of high angular resolution EBSD/Kikuchi patterns was used to extract lattice rotations with respect to a reference point in each EBSD map. These rotations were then used to calculate local lattice curvatures and then compute the surface GND densities. This technique can achieve a spatial resolution of  $\sim 50$  nanometres and a sensitivity above  $10^{12}$  lines/m<sup>2</sup> [55].

HR-EBSD measurements (Fig. 6) show the GND densities in the vicinity of an indent on each of the FeCr unimplanted surfaces. The average background GND density is stated below the corresponding maps. No differences between samples of different Cr concentrations could be found after accounting for the measurement uncertainties.

Electron channelling contrast imaging (ECCI) was also used to image and measure the dislocation density in the materials, as it can probe both GND and statistically stored dislocations (SSD). This method relies on the backscattered electron intensity signal while the electrons travel in the sample volume. The presence of lattice distortions, such as dislocations, alters the diffraction condition and thus allows defects to be imaged under specific conditions [56].

The ECCI maps of indents made in unimplanted Fe5Cr and Fe10Cr are shown in Fig. 7. Fe10Cr appears to exhibit slightly higher dislocation density than Fe5Cr in the region  $\sim 1$  to 2 microns away from the indent. Unfortunately, the backscatter contrast signal was not strong enough in the less deformed and undeformed regions to determine a background dislocation density. From these images, the pre-existing dislocation densities in unimplanted Fe5Cr and Fe10Cr seem to be quite low.

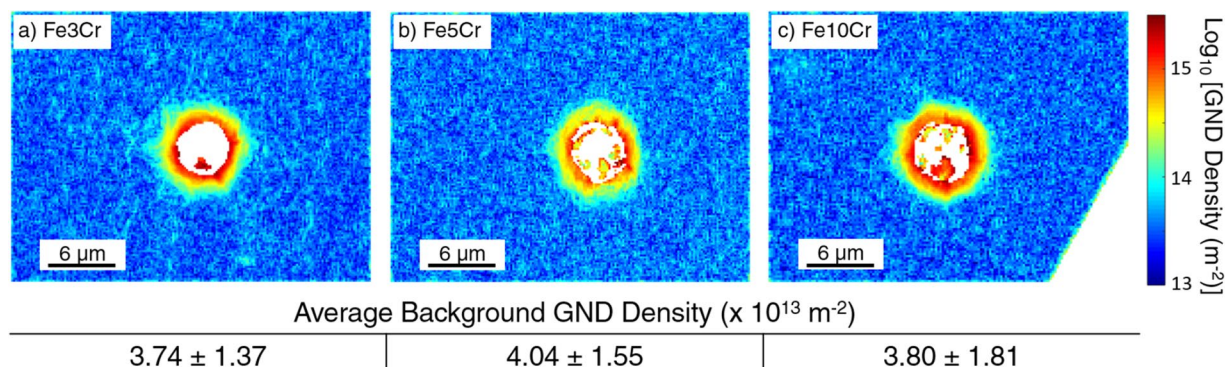


**Figure 6:** GND density distribution around spherical indents ( $R_{\text{eff}} = 5.03 \mu\text{m}$ ) in grains of near  $\langle 100 \rangle$  out-of-plane orientation on unimplanted (a) Fe3Cr, (b) Fe5Cr, and (c) Fe10Cr as measured by HR-EBSD. The average and standard deviation of the GND density are displayed below the corresponding maps

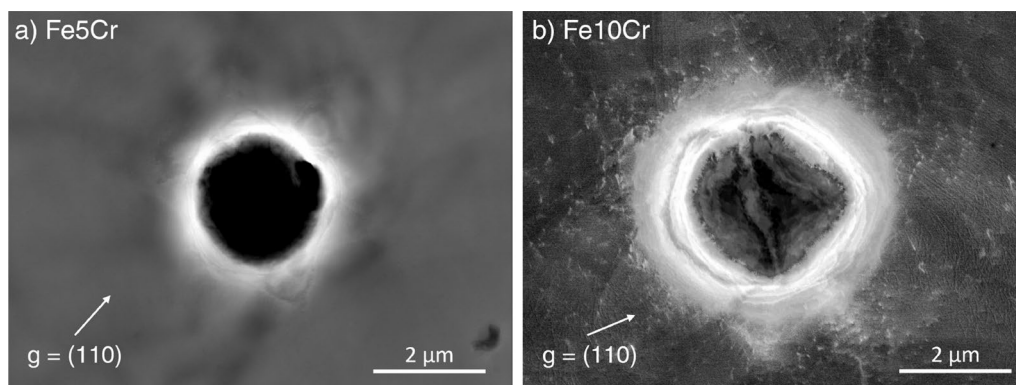


**Figure 7:** ECCI maps of regions around spherical indents ( $R_{\text{eff}} = 5.03 \mu\text{m}$ ) in grains of near  $\langle 111 \rangle$  out-of-plane orientation on unimplanted (a) Fe5Cr, and (b) Fe10Cr. Some dislocations can be observed around the indent in Fe10Cr but the contrast does not appear to be strong enough to observe dislocations in Fe5Cr.

### Progression of plasticity: indentation stress–strain curves

Nanoindentation measurements can also give insights into the progression of plasticity and yield in small sample volumes. The use of a spherical indenter tip can produce indentation stress–strain (ISS) curves analogous to those from bulk uniaxial tensile testing.

In our study, ISS curves were calculated using the protocols described in [57, 58]. Briefly, we started from the elastic contact described in Eq. 1, and defined contact radius  $a = \sqrt{Rh_e}$ . We then transformed Eq. 1 into a linear relationship during elastic contact. Indentation stress,  $\sigma_{\text{ind}}$ , and strain,  $\epsilon_{\text{ind}}$ , in the elastic regime, are defined as [57]:

$$\sigma_{\text{ind}} = \frac{P}{\pi a^2}; \quad \epsilon_{\text{ind}} = \frac{4}{3\pi} \frac{h_e}{a} \quad (6)$$

For elastic–plastic indentation,  $h_t$ , the total indentation depth, is used instead of  $h_e$ , the elastic indentation depth. In this picture, it is equivalent to idealising the indentation zone as a cylindrical region, of radius  $a$  and height  $\frac{3\pi}{4}a$ , being compressed by  $h_t$  [57].

The contact radius  $a$  was calculated from the measured stiffness,  $S = dP/dh_e$ , at each point in the loading curve:

$$a = \frac{S}{2E_r} \quad (7)$$

The indentation stress–strain (ISS) curves were calculated using Eqs. 6 and 7 in this study. However, ISS analysis cannot be applied to indentations made with the Berkovich tip as the spherical approximation of the tip shape is only valid for small indentation depths ( $< 20 \text{ nm}$ ). Beyond that depth, the self-similar geometry of the Berkovich tip means only one strain value is probed during indentation. For indents made with the 911 nm spherical tip, the pop-in stresses were so large that the analysis of the yield behaviour was difficult. At indentation depths greater than 200 nm, the deviation of tip shape from a perfect sphere

was also significant. Therefore, whilst the approximations made for the Berkovich tip and 911 nm spherical tip were appropriate for the pop-in analysis of the previous section, they cannot be used for ISS analysis. For the rest of this section, all analysis of ISS behaviour will focus solely on data obtained from indentations made with the 5.03  $\mu\text{m}$  spherical tip.

The ISS curves obtained from indentation with the 5.03  $\mu\text{m}$  tip are shown in [Fig. 8(a)–(c)]. The effects of pop-ins are clearly seen, with large elastic stresses in the ISS response before the flow portion proceeds at much lower stress levels. The trend of pop-ins, relating to the nucleation or unlocking of dislocations in the lattice, was extensively discussed in Sect. 2.1. The examination of ISS response for this section will focus on the flow, or plastic, portions which give insight into the propagation of dislocations in the material. Previous studies have shown that pop-ins do not affect the plastic behaviour in the ISS response as this depends on the mobility of dislocations rather than their nucleation [57, 59].

However, the presence of the pop-ins presents some difficulties in the analysis of the ISS response as they obstruct direct determination of the yield point and plastic behaviour immediately following yield. The method described in [60] was used to infer the yield point as the intersection of the elastic Hertzian response with a straight line fitted to the flow portion of the ISS curve. The yield strength is then defined using a 0.2% strain offset [Fig. 8(d)]. This is commonly used for defining yield strength in uniaxial tensile testing but has also been used in several studies to identify yield strength in nanoindentation measurements [58, 61, 62]. This back-extrapolation technique isolates the contributions to material yield strength due to dislocation propagation and multiplication, rather than dislocation nucleation [63–65].

The yield strength calculated from the ISS response increases monotonically with Cr content for all irradiation doses (Fig. 9). The origins of this, for tests performed at

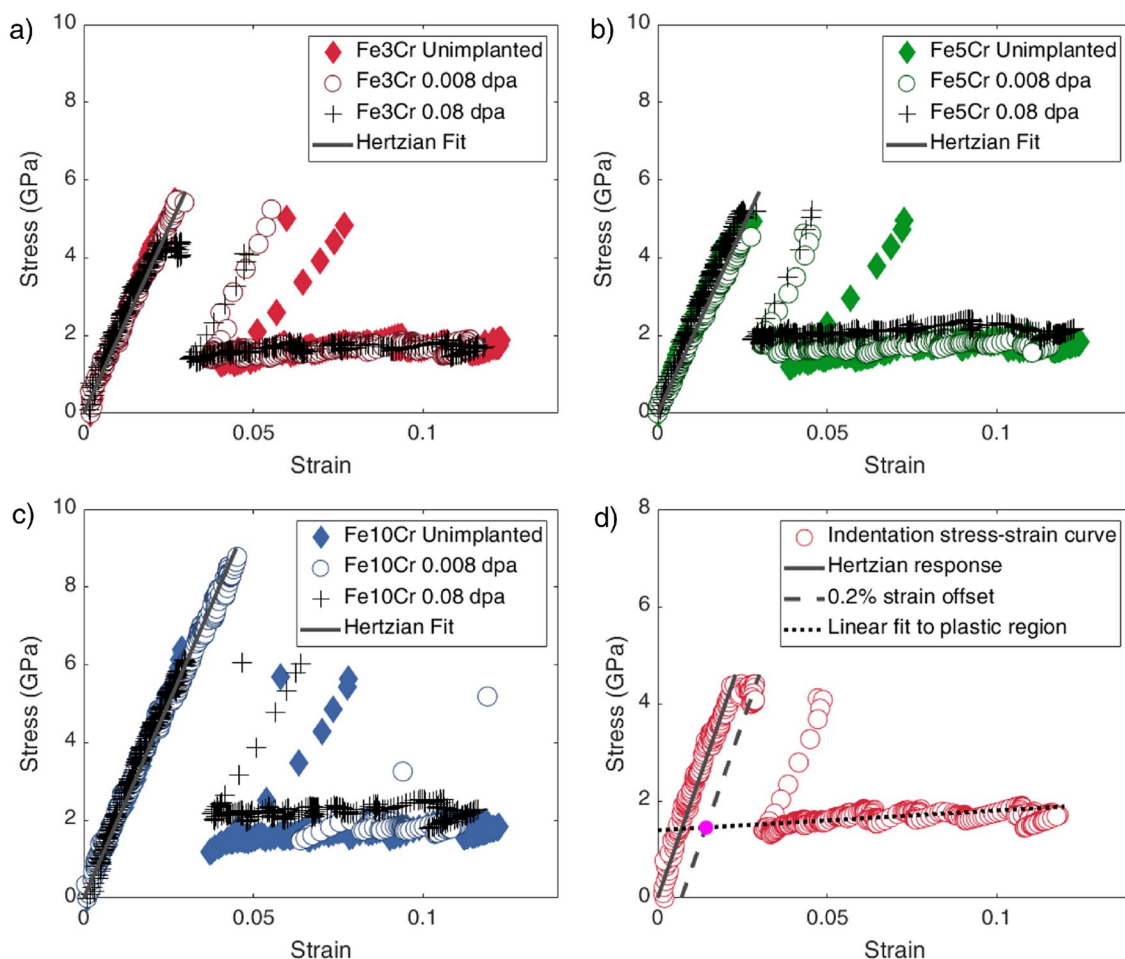


**Figure 8:** The indentation stress–strain (ISS) responses of (a) Fe3Cr, (b) Fe5Cr, and (c) Fe10Cr irradiated to different dose levels. The elastic portions of the curves are well-fitted to the prediction from Hertzian contact mechanics (Eq. 1) with the gradient equal to the reduced modulus of each sample. (d) The back-extrapolation of the yield strength (magenta point) as the intersection of the line which is a 0.2% strain offset from the Hertzian response (dashed grey line, offset exaggerated for clarity) and the line that is a linear fit of the plastic part of the ISS curve (black-dotted line).

the same temperature, is solid solution hardening, which is expected to increase with the square root of the solute concentration [73]. The rate of solid solution hardening in the yield strength of unirradiated FeCr is comparable to previous uniaxial tensile tests on single crystal FeCr samples [74] (detailed comparisons in Appendix A). The yield strength also increases monotonically with irradiation dose for all FeCr materials measured, which has been previously observed in other irradiated materials [15, 66].

The rate of yield strength increase between unimplanted and 0.008 dpa is lower for Fe10Cr compared to Fe3Cr and Fe5Cr, which would be consistent with a slightly higher pre-existing dislocation density in the Fe10Cr material, as discussed above. The higher rate of yield strength increase for Fe10Cr, compared to Fe3Cr and Fe5Cr, between 0.008 and 0.08 dpa, suggests increased retention of defects by the presence of Cr from a similar mechanism to irradiation hardening observed previously [24, 66].

These trends also agree with results from uniaxial stress–strain (USS) responses of neutron-irradiated Fe and FeCr [66, 67] (Fig. 9). This demonstrates the usefulness of high-throughput nanoindentation techniques to reveal insights into material behaviour. The discrepancy between the absolute values of the two studies can be attributed to several factors. The material on which USS response was measured was irradiated with neutrons at around 300 °C which could have partially annealed the material, compared to the materials in this study which were ion-irradiated at room temperature.

There have been numerous studies attempting to correlate indentation stress and strain values with the quantities obtained through bulk tensile testing. Huang et al. provide a good review of the literature [75]. Several factors lead to differences in the recorded stresses and strains, such that quantitative prediction of macroscopic stress–strain curves from nanoindentation remains challenging. An important factor is the role of lateral material constraint in indentation, which produces different



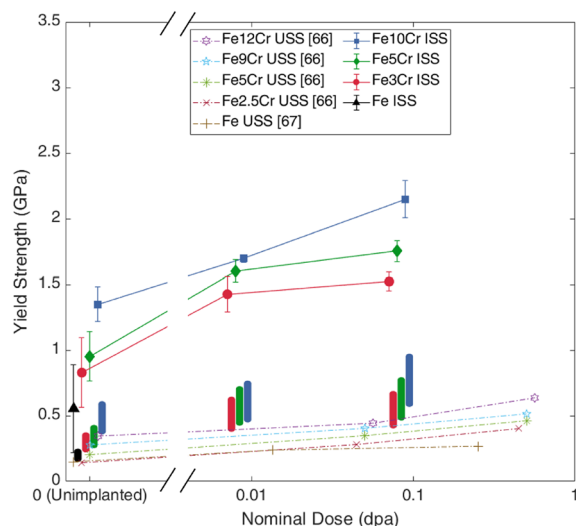


**Figure 9:** The yield strengths measured from the ISS responses of the Fe and FeCr materials as a function of dose in this study, using  $R_{\text{eff}} = 5.03 \mu\text{m}$  (markers with solid lines). The error bars show one standard deviation of the measurements. A comparison with yield strength measured from USS responses [66, 67] (markers with dashed lines) is shown. The elongated markers presented are the range of possible corrections to correlate the ISS and USS results based on studies in the literature [68–72]. Further details are given in the main text. Markers representing the same dose levels for each study have been spread laterally for visibility.

stress states compared to uniaxial tests [76]. A consequence of this is the difficulty in extracting exact contact depth of the indenter due to the deformed shape of the material around the indenter [72]. Another key difference is the heterogeneity of material microstructure. In nanoindentation, the deformation is probed in, essentially, a single crystal, whereas bulk tensile testing is more indicative of polycrystalline behaviour [66, 67, 77, 78]. A consequence of this is that orientation dependence may affect results of nanoindentation testing, but not bulk tensile testing. Furthermore, the indentation size effect, which is caused by both the presence of large plastic strain gradients and the nucleation of GNDs, is not found for bulk tensile testing [79]. For spherical indenters, this is a function of indenter size, rather than solely indentation depth as for sharp Berkovich indenters [80]. This size effect leads to a further increase the measured yield strength in nanoindentation compared to uniaxial testing [81, 82].

Various factors have been proposed to account for these differences between ISS and macroscopic stress–strain curves. For Fe in particular, there are a range of proposed ratios, between 2.2 to 3.8, for the conversion between indentation yield stress and tensile yield stress [68–72]. Figure 9 shows this range of ratios applied to our data for all samples. This brings the absolute values of the yield strengths from the ISS response closer to the macroscopic values reported in [66, 67]. Furthermore, the method of extrapolating the yield point may slightly

over-estimate the yield strength as the gradient of the ISS curve near the yield point is often higher than the gradient at larger strains [Fig. 8(d)].

The shape of the ISS curve in the flow portion gives insight into material work hardening. Past studies on irradiated Fe [67, 77, 78] have found that the work hardening response after yield is well-described by the Holloman relation:

$$\sigma = K\epsilon^n \quad (8)$$

where  $K$  is known as the strength coefficient and  $n$  is the work-hardening exponent. The hardening exponent is calculated for the samples in this study and compared with previous studies [67, 77, 78] in Fig. 10.

Reduced work-hardening capacity is evident with increased irradiation dose for all Cr% compositions studied. After irradiation to 0.08 dpa, all samples show a similar level of reduced work-hardening capacity. Considering that  $n$  increased with Cr content for unirradiated samples, it appears the effect of irradiation dominates in the changes to  $n$  compared to any pre-existing effects due to different Cr content. The rate of decrease of  $n$  with irradiation dose agree with trends in literature for Fe and FeCr [67, 77, 78].

In a previous study, analysis of the ISS response and TEM imaging of the plastic zone under indents in ion-irradiated Fe12Cr revealed that strain softening beyond the yield point arises from the annihilation of irradiation defects by reactions with glide dislocations [14, 28]. This has also been previously observed following bulk tensile testing of irradiated Fe [67, 83]. In this study the observed softening following deformation is also most likely due to the removal of defects by dislocation glide as slip steps in the pile-up topography are visible around indentations in the irradiated samples. The phenomenon of dislocation channelling leading to strain softening is common for many irradiated material systems [20, 84–86].

## Characterising behaviour in the initial stages of deformation

By combining the insights gathered from the nanoindentation pop-in trends and indentation stress–strain response studies, we can formulate a more coherent picture of the early stages of deformation and plasticity in irradiated FeCr.

In a volume of FeCr material free of pre-existing defects, homogeneous dislocation nucleation occurs when the applied stress exceeds the theoretical strength of the material. When the lattice is exposed to ion-irradiation, a dense population of nano-scale defects is formed [49, 52, 53]. In this study, the theoretical shear strengths of the materials were probed by studying maximum shear stress under a Berkovich indenter at the onset of plasticity (pop-ins). Our results show that even at low doses ( $\leq 0.08$  dpa), these act as local instabilities in the lattice, reducing

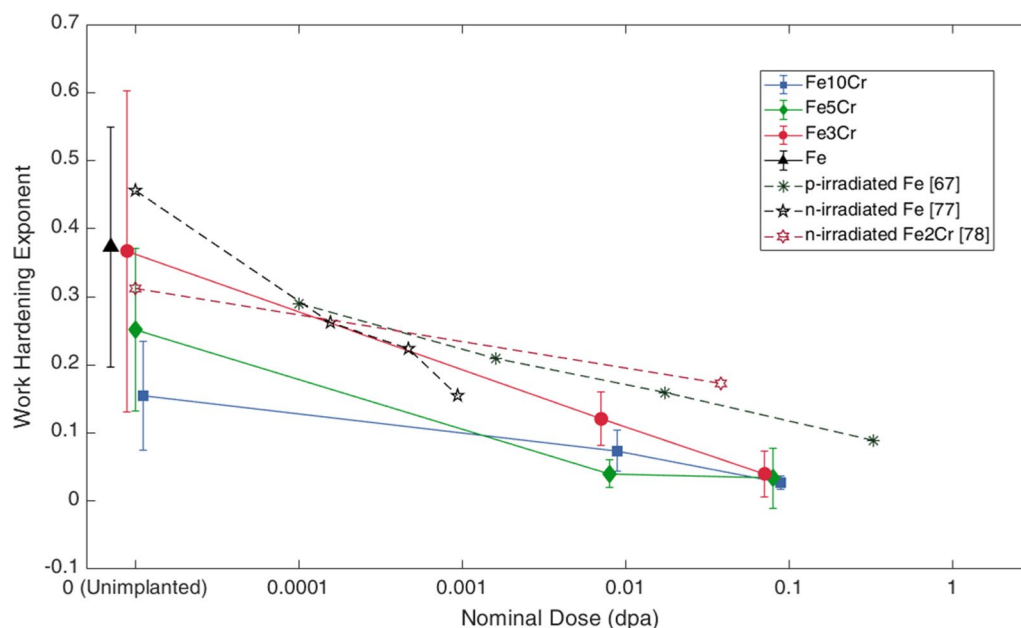


**Figure 10:** The work hardening exponent ( $n$ ) fitted from the flow portion from the ISS response of FeCr materials as a function of dose level. The error bars show one standard deviation of the measurements. Experimental results from proton-irradiated Fe [67], neutron-irradiated Fe [77], and neutron-irradiated Fe2Cr [78] are also shown for comparison.

the shear stress required to nucleate dislocations. Though the presence of Cr itself does not significantly affect the theoretical strength (Fig. 3), Cr enhance the effect of irradiation defects by increasing their retention [52, 53]. This causes the larger drop in shear stress required for dislocation nucleation following irradiation for higher Cr% materials (Fig. 4).

However, pre-existing heterogeneous dislocation sources, such as Frank–Read sources still play an important role in initiating plasticity in FeCr, as they generally require a lower stress for activation. One proposed mechanism for irradiation hardening is source hardening—whereby irradiation-induced defects cluster around pre-existing Frank–Read sources, causing the pinning or locking of dislocation lines. This increases the required stress to unlock these dislocations before they can multiply and initiate slip [87, 88]. By examining the initiation of plasticity with larger spherical tips (Fig. 5), we were able to probe the activation of pre-existing dislocations in irradiated FeCr. Our results suggest that the source hardening contributions of irradiation defects at the dose levels examined (0.008–0.08 dpa) are quite low as the required applied stress for plasticity initiation from pre-existing sources is not significantly affected following irradiation.

Once the pre-existing sources have been activated, the ease of dislocation propagation in the material can be determined through the yield strength. This behaviour was examined through the ISS responses from spherical nanoindentation, in particular the plastic portion. The presence of Cr, even in unirradiated materials, increases the yield strength due to

solid solution hardening. Following irradiation, the induced defects also act to hinder dislocation motion, further increasing the yield strength through friction hardening (also called lattice hardening) [63, 64, 89]. This finding is in line with early works on neutron irradiated iron and steels [90, 91]. Cr atoms further enhance the friction hardening from irradiation defects by increasing the retention of irradiation-induced defects, causing a larger rate of increase of yield strength following irradiation for materials with high Cr content (Fig. 9).

Irradiation also causes a reduction in work hardening capacity in FeCr due to the removal of irradiation defects by glide dislocations that form ‘easy glide’ dislocation channels, similar to other works on irradiated Fe [20, 84]. This study shows that the effect of irradiation-induced defects dominates the reduction in work hardening, as samples of all Cr% compositions have similar work hardening exponent following irradiation to 0.08 dpa. This shows that the increased retention of defects due to higher Cr content between Fe3Cr and Fe10Cr does not have a significant effect on the amount of strain softening experienced by irradiated FeCr.

It appears that the presence of Cr and irradiation defects mainly affects the initial stages of plasticity in irradiated FeCr by hindering dislocation motion. The effect of irradiation dose level is enhanced by the presence of Cr, due to increased retention of defects. This is significant in increasing the yield strength through friction hardening. To a lesser extent the presence of Cr and irradiation defects also hinders the nucleation of new dislocations. However, once the formation of dislocation channels

occurs in the irradiated material, the effect of irradiation dose is more dominant regardless of Cr content.

## Summary and conclusions

Fe3Cr, Fe5Cr, and Fe10Cr have been irradiated with 20 MeV  $\text{Fe}^{3+}$  ions to nominal doses of 0.008 and 0.08 dpa at room temperature. The effects of Cr content and irradiation dose on the initial stages of plasticity were studied using nanoindentation. We were able to separate the effects on initiation of plasticity and its early stages of progression using indenters of different sizes and shapes. We conclude the following from our findings:

- From studying pop-in trends in Berkovich tip indentation, the theoretical shear strength—how easily the crystal lattice shears, was probed. The presence of irradiation-induced defects reduces the theoretical shear strength of irradiated FeCr by reducing the barrier shear stress required for dislocation nucleation.
- The presence of Cr acts to increase the retention of irradiation-induced defects. This is the most prominent effect in controlling the reduction in the shear stress required to initiate plasticity from the nucleation of dislocations.
- The unlocking of pre-existing dislocation sources, such as from Frank–Read sources, still dominates the initiation of plasticity. This was studied through pop-in trends in spherical indentation. The presence of irradiation defects and Cr content did not significantly affect the operation of these pre-existing sources.
- From the indentation stress–strain responses, the yield strength of the FeCr materials were measured. This gave insight into how easily dislocations, once nucleated or unlocked, move through the materials. The yield strength increases with both Cr content and irradiation dose. The increased retention of irradiation-induced defects due to the presence of Cr further increased the yield strength. These trends agree with uniaxial stress–strain responses of neutron-irradiated FeCr material [66, 67].
- A decrease in work hardening is found following irradiation, which is quantitatively similar to previous irradiation studies [67, 77, 78]. However, following irradiation the effect of Cr content is small, while the irradiation-induced defect population seems to play a more dominant role in reducing work hardening capacity.
- This study highlights the usefulness of nanoindentation for gaining mechanistic insights into the competing effects that control the initiation and evolution of plasticity in irradiated materials.

## Materials and methods

### Materials and ion-implantation

This investigation considers the same samples as [24], which contains full details of their preparation and history. Briefly, polycrystalline samples of FeCr with 3, 5, and 10% Cr content (here referred to as Fe3Cr, Fe5Cr, and Fe10Cr, respectively) were manufactured under the European Fusion Development Agreement (EFDA) programme by induction melting and a series of forging and recrystallisation heat treatments [92]. The samples were mechanically ground with SiC paper then polished with diamond suspension and colloidal silica (0.04  $\mu\text{m}$ ). The final surface treatment performed was electropolishing with 5% perchloric acid in ethanol at  $-40^\circ\text{C}$  using a voltage of 28 V for 3–4 min.

Ion-implantation was performed with 20 MeV  $\text{Fe}^{3+}$  ions at room temperature using the tandem accelerator at the Helsinki Accelerator Laboratory. For each composition, samples were implanted to 2 nominal doses: 0.008 and 0.08 dpa (by averaging over the first 2  $\mu\text{m}$  of the dose profile), as calculated using the Quick K–P model in the SRIM code (20 MeV Fe ions on a Fe target with 40 eV displacement energy at normal incidence) [93]. The calculated damaged layer extends to 3  $\mu\text{m}$  below the sample surface (Fig. 2). Previous measurements using X-ray diffraction confirmed that the depth-dependent changes of strain in this layer match the predictions from SRIM [24]. One sample of each FeCr composition was set aside as an unimplanted reference. We note that the reported dose levels in this study differ from those reported in [24] even though the same samples were used. This is due to the difference in displacement energy used in the SRIM calculations. The study in [24] focused only on grains with  $\langle 100 \rangle$  out-of-plane orientation and thus the displacement energy used for Fe was lower. However, the present study considers a range of grain orientations and thus the international standard average value of 40 eV was used [94].

### Nanoindentation procedures

Nanoindentation experiments were performed using an MTS Nano Indenter XP. A Berkovich tip, and two spherical tips of nominal radii 1 and 5  $\mu\text{m}$  respectively were used. Continuous stiffness measurements (CSM) were conducted with a frequency of 45 Hz and a harmonic amplitude of 2 nm. The indenter, for all tip shapes, was loaded at a constant value of  $(dP/dt)/P = 0.05 \text{ s}^{-1}$ . Grains of near  $\langle 100 \rangle$ ,  $\langle 110 \rangle$  and  $\langle 111 \rangle$  out-of-plane orientations (within  $\pm 5^\circ$ ) were first identified by electron backscatter diffraction, then chosen for indentation. At least 10 indents were performed on each sample.

## Zero-point corrections for indentation stress–strain (ISS) curves

For the analysis of ISS curves, corrections for the point of effectively zero load and displacement were also made according to methods described in [95]. By considering the initial elastic segment ( $A \rightarrow B$ ) in the loading curve and using Hertz's theory, the stiffness can be written as:

$$S = \frac{3P}{2h_e} = \frac{3(\tilde{P} - P^*)}{2(\tilde{h}_e - h^*)} \quad (9)$$

where  $\tilde{P}$  and  $\tilde{h}_e$  are the measured load and displacement signals.  $P^*$  and  $h^*$  are the values of load and displacement at the point of effective initial contact. By rearranging Eq. 9, plotting  $\tilde{P} - \frac{2}{3}S\tilde{h}_e$  against  $S$  produced a linear relationship with a slope of  $-\frac{2}{3}h^*$  and a y-intercept of  $P^*$ . The values of  $P^*$  and  $h^*$  were then found by linear regression.

## High-resolution electron backscatter diffraction (HR-EBSD)

HR-EBSD measurements were performed on a Zeiss Merlin SEM (20 kV, 15 nA), with a Bruker eFlash detector system. The sample was tilted by 70° with respect to the electron beam, and a working distance of 18 mm was used. The measurements used a step size of 170 nm to ensure sufficient spatial coverage over the area around an indent while maintaining reasonable measurement times. Diffraction patterns were recorded at a resolution of 800 × 600 pixels. The cross-correlation analysis was carried out using a MATLAB-based code, originally written by Britton and Wilkinson [96].

## Electron channelling contrast imaging (ECCI)

ECCI measurements were performed on a Zeiss Crossbeam 540 SEM (30 kV, 10 nA), with a four-quadrant backscattered electron detector at nearly normal incidence to the electron beam direction.

## Acknowledgments

The authors would like to thank Robert Scales, Yun Deng, and Anna Kareer from the Department of Materials, University of Oxford for their assistance with ECCI image processing, pop-in searching algorithms, and ISS calculations.

## Funding

The authors acknowledge use of characterisation facilities within the David Cockayne Centre for Electron Microscopy, Department of Materials, University of Oxford,

alongside financial support provided by the Henry Royce Institute (Grant ref EP/R010145/1). KS acknowledges funding from the General Sir John Monash Foundation and the University of Oxford Department of Engineering Science. FH acknowledges funding from the European Research Council (ERC) under the European Union's Horizon 2020 research and innovation programme (Grant Agreement No. 714697). DEJA acknowledges funding from EPSRC Grant EP/P001645/1.

## Data availability

All data, raw and processed, as well as the processing and plotting scripts are available at: <https://doi.org/10.5287/bodleian:Nom6Ygbbz>.

## Declarations

**Conflict of interest** The authors have no relevant financial or non-financial interests to disclose.

## Open Access

This article is licensed under a Creative Commons Attribution 4.0 International License, which permits use, sharing, adaptation, distribution and reproduction in any medium or format, as long as you give appropriate credit to the original author(s) and the source, provide a link to the Creative Commons licence, and indicate if changes were made. The images or other third party material in this article are included in the article's Creative Commons licence, unless indicated otherwise in a credit line to the material. If material is not included in the article's Creative Commons licence and your intended use is not permitted by statutory regulation or exceeds the permitted use, you will need to obtain permission directly from the copyright holder. To view a copy of this licence, visit <http://creativecommons.org/licenses/by/4.0/>.

## Appendix

A comparison is made between the solid solution hardening from the indentation yield strength results of this study and uniaxial tensile tests performed by Horne et al. [74] on single crystal samples of Fe and FeCr at 300 K. The amount of hardening between Fe and Fe-11.9%Cr (in this study Fe10Cr) is similar between the two studies (Fig. 11). It is unclear why there is a reduction in CRSS in the single crystal study from Fe to Fe-2.1%Cr and Fe to Fe-4.8%Cr. The overall slope of the fitting hardening rate is similar.



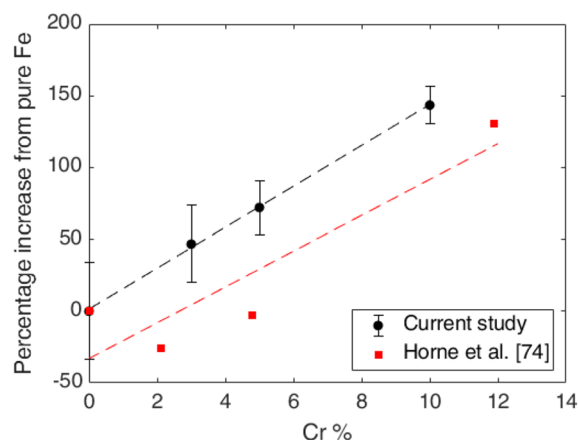


**Figure 11:** The rate of yield stress increase (relative to the yield stress of pure Fe samples in the respective studies) of values obtained via uniaxial tensile testing (red squares) from Horne et al. [74] compared to those obtained via ISS analysis in this study (black circles).

## References

1. N. Baluc, R. Schäublin, P. Spätig, M. Victoria, On the potentiality of using ferritic/martensitic steels as structural materials for fusion reactors. *Nucl. Fusion* **44**(1), 56–61 (2004)
2. K. Ehrlich, Materials research towards a fusion reactor. *Fusion Eng. Des.* **56–57**, 71–82 (2001)
3. A.A.F. Tavassoli, Present limits and improvements of structural materials for fusion reactors—a review. *J. Nucl. Mater.* **302**(2–3), 73–88 (2002)
4. F.A. Garner, M.B. Toloczko, B.H. Sencer, Comparison of swelling and irradiation creep behavior of fcc-austenitic and bcc-ferritic/martensitic alloys at high neutron exposure. *J. Nucl. Mater.* **276**(1), 123–142 (2000)
5. M. Lambrecht, L. Malerba, Positron annihilation spectroscopy on binary Fe–Cr alloys and ferritic/martensitic steels after neutron irradiation. *Acta Mater.* **59**(17), 6547–6555 (2011)
6. L. Malerba, G. Bonny, D. Terentyev, E.E. Zhurkin, M. Hou, K. Vörtler, K. Nordlund, Microchemical effects in irradiated Fe–Cr alloys as revealed by atomistic simulation. *J. Nucl. Mater.* **442**(1–3), 486–498 (2013)
7. F. Granberg, J. Byggmästar, K. Nordlund, Defect accumulation and evolution during prolonged irradiation of Fe and FeCr alloys. *J. Nucl. Mater.* **528**, 151 (2020)
8. G.S. Was, Challenges to the use of ion irradiation for emulating reactor irradiation. *J. Mater. Res.* **30**(9), 1158–1182 (2015)
9. G.S. Was, Z. Jiao, E. Getto, K. Sun, A.M. Monterrosa, S.A. Maloy, O. Anderoglu, B.H. Sencer, M. Hackett, Emulation of reactor irradiation damage using ion beams. *Scripta Mater.* **88**, 33–36 (2014)
10. G.S. Was, R.S. Averback, Radiation damage using ion beams. *Compr. Nucl. Mater.* **1**, 195–221 (2012)
11. D.R. Mason, A.E. Sand, X. Yi, S.L. Dudarev, Direct observation of the spatial distribution of primary cascade damage in tungsten. *Acta Mater.* **144**, 905–917 (2018)
12. X. Yi, A.E. Sand, D.R. Mason, M.A. Kirk, S.G. Roberts, K. Nordlund, S.L. Dudarev, Direct observation of size scaling and elastic interaction between nano-scale defects in collision cascades. *Europhys. Lett.* **110**(3), 36001 (2015)
13. C. Heintze, F. Bergner, M. Hernández-Mayoral, Ion-irradiation-induced damage in Fe–Cr alloys characterized by nanoindentation. *J. Nucl. Mater.* **417**(1–3), 980–983 (2011)
14. A.J. Bushby, S.G. Roberts, C.D. Hardie, Nanoindentation investigation of ion-irradiated Fe–Cr alloys using spherical indenters. *J. Mater. Res.* **27**(1), 85–90 (2012)
15. S. Pathak, S.R. Kalidindi, J.S. Weaver, Y. Wang, R.P. Doerner, N.A. Mara, Probing nanoscale damage gradients in ion-irradiated metals using spherical nanoindentation. *Sci. Rep.* **7**(1), 1–12 (2017)
16. D. Kiener, A.M. Minor, O. Anderoglu, Y. Wang, S.A. Maloy, P. Hosemann, Application of small-scale testing for investigation of ion-beam-irradiated materials. *J. Mater. Res.* **27**(21), 2724–2736 (2012)
17. X. Xiao, Yu. Long, Nano-indentation of ion-irradiated nuclear structural materials: a review. *Nucl. Mater. Energy* **22**, 100721 (2020)
18. M. Victoria, N. Baluc, C. Bailat, Y. Dai, M.I. Luppó, R. Schaublin, B.N. Singh, The microstructure and associated tensile properties of irradiated fcc and bcc metals. *J. Nucl. Mater.* **276**(1–3), 114–122 (2000)
19. K. Suganuma, H. Kayano, Irradiation hardening of Fe–Cr alloys. *J. Nucl. Mater.* **118**(2–3), 234–241 (1983)
20. S.J. Zinkle, B.N. Singh, Microstructure of neutron-irradiated iron before and after tensile deformation. *J. Nucl. Mater.* **351**(1–3), 269–284 (2006)
21. E.A. Little, Neutron-irradiation hardening in irons and ferritic steels. *Int. Metals Rev.* **21**(1), 25–60 (1976)
22. C.D. Hardie, S.G. Roberts, Nanoindentation of model Fe–Cr alloys with self-ion irradiation. *J. Nucl. Mater.* **433**(1–3), 174–179 (2013)
23. S. Li, Y. Wang, X. Dai, F. Liu, J. Li, X. Wang, Evaluation of hardening behaviors in ion-irradiated Fe–9Cr and Fe–20Cr alloys by nanoindentation technique. *J. Nucl. Mater.* **478**, 50–55 (2016)
24. K. Song, S. Das, A. Reza, N.W. Phillips, R. Xu, H. Yu, K. Mizohata, D.E.J. Armstrong, F. Hofmann, Characterising ion-irradiated FeCr: hardness, thermal diffusivity and lattice strain. *Acta Materialia* **201**, 535–546 (2020)
25. C.D. Hardie, S.G. Roberts, A.J. Bushby, Understanding the effects of ion irradiation using nanoindentation techniques. *J. Nucl. Mater.* **462**, 391–401 (2015)
26. C.D. Hardie, G.R. Odette, Y. Wu, S. Akhmaliev, S.G. Roberts, Mechanical properties and plasticity size effect of Fe–6Cr

- irradiated by Fe ions and by neutrons. *J. Nucl. Mater.* **482**, 236–247 (2016)
27. D.E.J. Armstrong, C.D. Hardie, J.S.K.L. Gibson, A.J. Bushby, P.D. Edmondson, S.G. Roberts, Small-scale characterisation of irradiated nuclear materials: part II nanoindentation and micro-cantilever testing of ion irradiated nuclear materials. *J. Nucl. Mater.* **462**, 374–381 (2015)
28. C.D. Hardie, S.G. Roberts, A.J. Bushby, *Mechanical Behavior of Ion-irradiated Fe–Cr Alloys Investigated by Spherical Indentation* (Cambridge University Press, Cambridge, 2012), pp. 1–6
29. P.M. Derlet, S.L. Dudarev, Microscopic structure of a heavily irradiated material. *Phys. Rev. Mater.* **4**(2), 023605 (2020)
30. X. Hu, D. Xu, T.S. Byun, B.D. Wirth, Modeling of irradiation hardening of iron after low-dose and low-temperature neutron irradiation. *Modell. Simul. Mater. Sci. Eng.* **22**(6), 065002 (2014)
31. K. Papamihail, K. Mergia, F. Ott, Y. Serruys, T. Speliotis, G. Apostolopoulos, S. Messoloras, Magnetic effects induced by self-ion irradiation of Fe films. *Phys. Rev. B* **93**(10), 100404 (2016)
32. B.A. Gurovich, E.A. Kuleshova, D.A. Mal'tsev, Y.M. Semchenkov, A.S. Frolov, Y.I. Shtrombakh, A.V. Shutikov, Mechanism of change in VVER-440, -1000 Vessel material properties in irradiation-recovery annealing-irradiation cycle. *At. Energy* **125**(2), 95–102 (2018)
33. A.R. Allnatt, A.B. Lidiard, *Atomic Transport in Solids* (Cambridge University Press, Cambridge, 1993)
34. K.L. Johnson, *Contact Mechanics* (Cambridge University Press, Cambridge, 1987)
35. C. Anthony, *Fischer-Cripps. Nanoindentation*, 3rd edn. (Springer, New York, 2011)
36. H.M. Ledbetter, R.P. Reed, Elastic properties of metals and alloys, I. Iron, nickel, and iron–nickel alloys. *J. Phys. Chem. Ref. Data* **2**(3), 531–618 (1973)
37. A. Leitner, V. Maier-Kiener, D. Kiener, Essential refinements of spherical nanoindentation protocols for the reliable determination of mechanical flow curves. *Mater. Des.* **146**, 69–80 (2018)
38. X. Xiao, Yu. Long, A unified statistical model for indentation pop-in: effects of indenter radius and microstructure density on the transition from homogeneous nucleation to heterogeneous nucleation to bulk plasticity. *Int. J. Plast.* **141**, 102980 (2021)
39. S. Shim, H. Bei, E.P. George, G.M. Pharr, A different type of indentation size effect. *Scripta Mater.* **59**(10), 1095–1098 (2008)
40. B.D. Beake, S. Goel, Incipient plasticity in tungsten during nanoindentation: dependence on surface roughness, probe radius and crystal orientation. *Int. J. Refract. Metal Hard Mater.* **75**, 63–69 (2018)
41. J.R. Morris, H. Bei, G.M. Pharr, E.P. George, Size effects and stochastic behavior of nanoindentation pop in. *Phys. Rev. Lett.* **106**(16), 165502 (2011)
42. T.H. Ahn, C.S. Oh, K. Lee, E.P. George, H.N. Han, Relationship between yield point phenomena and the nanoindentation pop-in behavior of steel. *J. Mater. Res.* **27**(1), 39–44 (2012)
43. L. Casillas-Trujillo, X. Liubin, X. Haixuan, Compositional effects on ideal shear strength in Fe–Cr alloys. *J. Alloy. Compd.* **720**, 466–472 (2017)
44. C.R. Krenn, D. Roundy, M.L. Cohen, D.C. Chrzan, J.W. Morris, Connecting atomistic and experimental estimates of ideal strength. *Phys. Rev. B* **65**(13), 1–4 (2002)
45. Y. Song, D.S. Xu, R. Yang, D. Li, W.T. Wu, Z.X. Guo, Theoretical study of the effects of alloying elements on the strength and modulus of  $\beta$ -type bio-titanium alloys. *Mater. Sci. Eng. A* **260**(1–2), 269–274 (1999)
46. Y.M. Huang, J.C.H. Spence, O.F. Sankey, The effect of impurities on the ideal tensile strength of silicon. *Philos. Mag. A* **70**(1), 53–62 (1994)
47. G.R. Speich, A.J. Schwoeble, W.C. Leslie, Elastic constants of binary iron-base alloys. *Metall. Trans.* **3**(8), 2031–2037 (1972)
48. C. Heintze, F. Bergner, A. Ulbricht, Characterization of Fe–Cr alloys using SANS, nanoindentation and ultrasound. (2009)
49. R. Schäublin, B. Décamps, A. Prokhotseva, J.F. Löffler, On the origin of primary  $1/2 a_0 \langle 111 \rangle$  and  $a_0 \langle 100 \rangle$  loops in irradiated Fe(Cr) alloys. *Acta Materialia* **133**, 427–439 (2017)
50. K. Jin, Y. Xia, M. Crespillo, H. Xue, Y. Zhang, Y.F. Gao, H. Bei, Quantifying early stage irradiation damage from nanoindentation pop-in tests. *Scripta Mater.* **157**, 49–53 (2018)
51. H. Bei, Y.Z. Xia, R.I. Barabash, Y.F. Gao, A tale of two mechanisms: strain-softening versus strain-hardening in single crystals under small stressed volumes. *Scripta Mater.* **110**, 48–52 (2016)
52. Z. Yao, M. Hernández-Mayoral, M.L. Jenkins, M.A. Kirk, Heavy-ion irradiations of Fe and Fe–Cr model alloys Part 1: damage evolution in thin-foils at lower doses. *Philos. Mag.* **88**(21), 2851–2880 (2008)
53. M. Hernandez-Mayoral, Z. Yao, M.L. Jenkins, M.A. Kirk, Heavy-ion irradiations of Fe and Fe–Cr model alloys Part 2: damage evolution in thin-foils at higher doses. *Philos. Mag.* **88**(21), 2881–2897 (2008)
54. D. Wallis, L.N. Hansen, T.B. Britton, A.J. Wilkinson, Geometrically necessary dislocation densities in olivine obtained using high-angular resolution electron backscatter diffraction. *Ultramicroscopy* **168**, 34–45 (2016)
55. J. Jiang, T.B. Britton, A.J. Wilkinson, Measurement of geometrically necessary dislocation density with high resolution electron backscatter diffraction: Effects of detector binning and step size. *Ultramicroscopy* **125**, 1–9 (2013)
56. S. Zaeferrer, N.N. Elhami, Theory and application of electron channelling contrast imaging under controlled diffraction conditions. *Acta Materialia* **75**, 20–50 (2014)
57. S. Pathak, S.R. Kalidindi, Spherical nanoindentation stress–strain curves. *Mater. Sci. Eng.* **91**, 1–36 (2015)
58. D.K. Patel, S.R. Kalidindi, Correlation of spherical nanoindentation stress–strain curves to simple compression stress–strain curves for elastic–plastic isotropic materials using finite element models. *Acta Mater.* **112**, 295–302 (2016)

59. S. Pathak, D. Stojakovic, R. Doherty, S.R. Kalidindi, Importance of surface preparation on the nano-indentation stress-strain curves measured in metals. *J. Mater. Res.* **24**(3), 1142–1155 (2009)
60. T. Zhu, A. Bushby, D. Dunstan, Size effect in the initiation of plasticity for ceramics in nanoindentation. *J. Mech. Phys. Solids* **56**(4), 1170–1185 (2008)
61. J.S. Weaver, A. Khosravani, A. Castillo, S.R. Kalidindi, High throughput exploration of process-property linkages in Al-6061 using instrumented spherical microindentation and micro-structurally graded samples. *Integr. Mater. Manuf. Innov.* **5**(1), 192–211 (2016)
62. J.S. Weaver, M.W. Priddy, D.L. McDowell, S.R. Kalidindi, On capturing the grain-scale elastic and plastic anisotropy of alpha-Ti with spherical nanoindentation and electron back-scattered diffraction. *Acta Mater.* **117**, 23–34 (2016)
63. M.J. Makin, F.J. Minter, Irradiation hardening in copper and nickel. *Acta Metall.* **8**(10), 691–699 (1960)
64. K.L. Murty, D.J. Oh, Friction and source hardening in irradiated mild steel. *Scripta Metallurgica* **17**(3), 317–320 (1983)
65. S.B. Kass, K.L. Murty, Effect of neutron irradiation on mechanical properties of ferritic steels. *Annual meeting and exhibition of the Minerals, Metals and Materials Society (TMS), Las Vegas, NV (United States), 12-16 Feb 1995*, pp. 27–35, (1995)
66. M. Matijasevic, A. Almazouzi, Effect of Cr on the mechanical properties and microstructure of Fe–Cr model alloys after n-irradiation. *J. Nucl. Mater.* **377**(1), 147–154 (2008)
67. M.I. Luppó, C. Bailat, R. Schäublin, M. Victoria, Tensile properties and microstructure of 590 MeV proton-irradiated pure Fe and a Fe–Cr alloy. *J. Nucl. Mater.* **283**, 483–487 (2000)
68. D. Tabor, A simple theory of static and dynamic hardness. *Proc. R. Soc. Lond.* **192**(1029), 247–274 (1948)
69. E.G. Herbert, E.G. Herbert, G.M. Pharr, W.C. Oliver, J.L. Hay, B.N. Lucas, On the measurement of stress-strain curves by spherical indentation. *Thin Solid Films* **398**(399), 331–335 (2001)
70. S. Basu, A. Moseson, M.W. Barsoum, On the determination of spherical nanoindentation stress-strain curves. *J. Mater. Res.* **21**(10), 2628–2637 (2006)
71. B.R. Donohue, A. Ambrus, S.R. Kalidindi, Critical evaluation of the indentation data analyses methods for the extraction of isotropic uniaxial mechanical properties using finite element models. *Acta Mater.* **60**(9), 3943–3952 (2012)
72. X. Baoxing, X. Chen, Determining engineering stress-strain curve directly from the load-depth curve of spherical indentation test. *J. Mater. Res.* **25**(12), 2297–2307 (2010)
73. G.E. Dieter, *Mechanical Metallurgy* (McGraw-Hill Book Company Inc., Irvine, 1961)
74. G.T. Horne, R.B. Roy, H.W. Paxton, Tensile properties of single crystals of iron–chromium alloys. *J. Iron Steel Inst.* **201**, 161–167 (1963)
75. F.Y. Huang, Y.W. Liu, J.C. Kuo, Uncertainties in the representative indentation stress and strain using spherical nanoindentation. *Appl. Nanosci.* **11**(3), 895–909 (2021)
76. K.L. Johnson, The correlation of indentation experiments. *J. Mech. Phys. Solids* **18**(2), 115–126 (1970)
77. I.L. Mogford, D. Hull, Effect of temperature and neutron irradiation on yield and work hardening in iron. *J. Iron Steel Inst.* **201**, 55–60 (1963)
78. A. Okada, N. Kawaguchi, M.L. Hamilton, K. Hamada, T. Yoshiie, I. Ishida, E. Hirota, Mechanical property change in neutron irradiated Fe–Cr and Fe–Mn alloys, and their defect structures. *J. Nucl. Mater.* **212–215**, 382–387 (1994)
79. W.D. Nix, H. Gao, Indentation size effects in crystalline materials: a law for strain gradient plasticity. *J. Mech. Phys. Solids* **46**(3), 411–425 (1998)
80. J.G. Swadener, E.P. George, G.M. Pharr, The correlation of indentation size effect experiments with pyramidal and spherical indenters. *MRS Online Proc. Library (OPL)* **695**, 451–456 (2001)
81. J.G. Swadener, E.P. George, G.M. Pharr, The correlation of the indentation size effect measured with indenters of various shapes. *J. Mech. Phys. Solids* **50**(4), 681–694 (2002)
82. Y.V. Milman, A.A. Golubenko, S.N. Dub, Indentation size effect in nanohardness. *Acta Mater.* **59**(20), 7480–7487 (2011)
83. B.N. Singh, A. Horsewell, P. Toft, Effects of neutron irradiation on microstructure and mechanical properties of pure iron. *J. Nucl. Mater.* **271–272**, 97–101 (1999)
84. S.M. Ohr, Work hardening characteristics of neutron irradiated iron. *Scr. Metall.* **2**(4), 213–216 (1968)
85. T.S. Byun, N. Hashimoto, K. Farrell, E.H. Lee, Characteristics of microscopic strain localization in irradiated 316 stainless steels and pure vanadium. *J. Nucl. Mater.* **349**(3), 251–264 (2006)
86. N. Hashimoto, T.S. Byun, K. Farrell, S.J. Zinkle, Deformation microstructure of neutron-irradiated pure polycrystalline metals. *J. Nucl. Mater.* **329–333**(1–3 PART B), 947–952 (2004)
87. G. Was, Irradiation Hardening and Deformation. In *Fundamentals of Radiation Materials Science*. Springer, Berlin (2007)
88. F. Bergner, M. Hernández-Mayoral, C. Heintze, M.J. Konstantinović, L. Malerba, C. Pareige, TEM observation of loops decorating dislocations and resulting source hardening of neutron-irradiated Fe–Cr alloys. *Metals* **10**(1), 147 (2020)
89. K.L. Murty, Role and significance of source hardening in radiation embrittlement of iron and ferritic steels. *J. Nucl. Mater.* **270**(1–2), 115–128 (1999)
90. D. Hull, I.L. Mogford, Ductile-brittle transition in steels irradiated with neutrons. *Philos. Mag.* **3**(35), 1213–1222 (1958)

91. J.G.Y. Chow, S.B. Mcrickard, Effects on neutron irradiation on the yield strength and grain size relationship in iron and iron-carbon alloys. *Philos. Mag.* **8**(96), 2097–2099 (1963)
92. J.L. Coze, *Procurement of pure Fe metal and Fe-based alloys with controlled chemical alloying element contents and microstructure* (Technical report, ARMINES Ecole Nationale Supérieure des Mines, 2007)
93. J.F. Ziegler, M.D. Ziegler, J.P. Biersack, SRIM The stopping and range of ions in matter. *Nucl. Instrum. Methods Phys. Res. Sect. B* **268**(11–12), 1818–1823 (2010)
94. ASTM E521. Standard Practice for Investigating the Effects of Neutron Radiation Damage Using Charged-Particle Irradiation. In *Annual Book of ASTM Standards*, volume 12.02. ASTM International, West Conshohocken, PA, (2016)
95. S.R. Kalidindi, S. Pathak, Determination of the effective zero-point and the extraction of spherical nanoindentation stress-strain curves. *Acta Mater.* **56**(14), 3523–3532 (2008)
96. T.B. Britton, A.J. Wilkinson, High resolution electron backscatter diffraction measurements of elastic strain variations in the presence of larger lattice rotations. *Ultramicroscopy* **114**, 82–95 (2012)